



HAL
open science

Removal of oxygenated volatile organic compounds by catalytic oxidation over Zr-Ce-Mn catalysts

Saïd Azalim, Manuel Franco, Rachid Brahmi, Jean-Marc Giraudon,
Jean-Francois Lamonier

► **To cite this version:**

Saïd Azalim, Manuel Franco, Rachid Brahmi, Jean-Marc Giraudon, Jean-Francois Lamonier. Removal of oxygenated volatile organic compounds by catalytic oxidation over Zr-Ce-Mn catalysts. *Journal of Hazardous Materials*, 2011, *Journal of Hazardous Materials*, 188, pp.422-427. 10.1016/j.jhazmat.2011.01.135 . hal-04135520

HAL Id: hal-04135520

<https://hal.univ-lille.fr/hal-04135520>

Submitted on 21 Jun 2023

HAL is a multi-disciplinary open access archive for the deposit and dissemination of scientific research documents, whether they are published or not. The documents may come from teaching and research institutions in France or abroad, or from public or private research centers.

L'archive ouverte pluridisciplinaire **HAL**, est destinée au dépôt et à la diffusion de documents scientifiques de niveau recherche, publiés ou non, émanant des établissements d'enseignement et de recherche français ou étrangers, des laboratoires publics ou privés.

1 **Removal of oxygenated volatile organic compounds by catalytic oxidation**
2 **over Zr-Ce-Mn catalysts**

3
4
5
6
7
8 **Saïd Azalim^{a,b}, Manuel Franco^a, Rachid Brahmi^b, Jean-Marc Giraudon^a and Jean-**
9 **François Lamonier^{a*}**

10
11
12 *^aUniv Lille Nord de France, USTL, Unité de Catalyse et de Chimie du Solide, UMR CNRS*
13 *8181, 59652 Villeneuve d'Ascq, France*

14
15
16
17 *^bUCD, Laboratoire de Catalyse et de Corrosion des Matériaux, Faculté des Sciences, 24000*
18 *El Jadida, Morocco*

19
20
21
22 **Corresponding author: Fax +33320436561, jean-francois.lamonier@univ-lille1.fr*

23
24
25
26
27 **Abstract:** The composition-activity relationship of Zr-Ce-Mn-O materials was investigated
28
29 for the catalytic removal of Oxygenated Volatile Organic Compounds (OVOC) emitted by
30
31 stationary sources. Using a sol-gel method, very high surface specific areas, small crystallite
32
33 sizes and high redox properties were obtained for $Zr_{0.4}Ce_{0.6-x}Mn_xO_2$ catalytic systems after
34
35 calcination at 500°C. The textural and redox properties were improved when Mn content
36
37 increased in the material, especially for $x = 0.36$. As a result the most active and selective
38
39 catalyst in the butanol (model of OVOC) oxidation was obtained for the nominal composition
40
41 $Zr_{0.4}Ce_{0.24}Mn_{0.36}O_2$ due to a high oxygen mobility and surface Mn^{4+} concentration.

42
43
44
45
46
47
48
49 **Keywords:** VOC ; catalytic oxidation ; Zr-Ce-Mn mixed oxides ; butanol
50
51
52
53
54
55
56
57
58
59
60
61
62
63
64
65

24 Introduction

25 Volatile Organic compounds (or VOCs) are major air pollutants and their treatment by
26 catalytic oxidation is one of the most promising ways to reduce these pollutants. This
27 technique has the advantage of operating at low temperatures (200-500°C), thus leading to
28 low NO_x formation. Noble-metal oxide catalysts using supported Pt or Pd are conventionally
29 used [1,2]. However, attention has also been given to transition metals due to the limited
30 availability and high cost of noble metals [3,4]. To improve the performance of transition
31 metal oxide catalysts, the dispersion of active metallic species must be optimized by using a
32 suitable support [5] and/or a synergistic effect between different species must be achieved
33 through the formation of mixed oxides. Among the transition metal oxides, mixed-valent
34 manganese oxide materials are good candidates for oxygenated VOC removal. The γ -MnO₂
35 phase has been reported to be more active than β -MnO₂ or Mn₂O₃ in the oxidation of ethanol
36 [6]. In the same reaction, K-Mn oxides (cryptomelane type) are also reported because of the
37 presence of Mn⁴⁺/Mn³⁺ ions and the hydrophobic character of the solid [7]. Due to the
38 favorable properties of ceria in oxidation catalysis, the Mn-Ce-O catalytic system has also
39 been examined in the VOC removal by catalytic wet or dry oxidation [8-11]. MnO_x-CeO₂
40 mixed oxides had much higher catalytic activity than that of pure MnO_x and CeO₂ owing to
41 the formation of the solid solution between manganese and cerium oxides [12]. But the
42 interactions between MnO_x and CeO₂ vary with the composition and the optimum Mn/Ce
43 ratio depends on (i) the catalyst synthesis method and (ii) the nature of the pollutant to be
44 destroyed. Besides it is well known that formation of mixed oxides of ceria with Zr⁴⁺
45 enhanced oxygen storage properties of ceria and the so-formed mixed oxides exhibited good
46 thermal stability [13].

47 Butanol enters the environment from either natural sources or during its production, transport,
48 storage and use as a chemical intermediate and a solvent. The primary route for entering the

1
2
3
4
5
6
7
8
9
10
11
12
13
14
15
16
17
18
19
20
21
22
23
24
25
26
27
28
29
30
31
32
33
34
35
36
37
38
39
40
41
42
43
44
45
46
47
48
49
50
51
52
53
54
55
56
57
58
59
60
61
62
63
64
65
66
67
68
69
70
71
72

environment is the release to the atmosphere when used as a solvent for paints, coatings, varnishes, resins, gums, vegetable oils etc. Occupational exposure may occur through inhalation and dermal contact with this compound at workplaces where n-butanol is produced or used. n-butanol is not classifiable as to human and animal carcinogenicity [14]. However a 10 year study, conducted of men exposed to this compound (>200 ppm of n-butanol) in an industrial setting, revealed ocular symptoms included a burning sensation, blurring of vision, lachrymation, and photophobia [15]. Animal exposed to n-butanol in air may manifest ataxia, central nervous system depression, prostration. Deaths from acute overexposure are believed due to respiratory failure. Guinea pigs exposed to 100 ppm, (4hr/day ; 6 day/week for 64 exposures) showed a decrease in number of red blood count. Rats subjected to 130 hours of total exposure to a concentration of 8000 ppm showed CNS depression [15].

In spite of numerous studies covering catalytic oxidation of a wide range of VOCs, only few reports deal with catalytic total oxidation of n-butanol in air, in order to remove this hazardous compound [16-18]. P. Papaefthimiou et al. [16,17] have studied the oxidation of a VOC mixture which includes ethyl acetate, benzene and n-butanol. Butanol has been chosen as representative model compounds for alcohols. The main scope of this work was to determine the most active group VIII metal catalysts for the removal of this VOC mixture. Among them Pt and Pd supported on alumina [16] and titania [17] were the most active metals for benzene and butanol oxidation. V₂O₅-WO₃/TiO₂ catalyst, recognized as combining high activity and selectivity together with a strong stability in Cl₂-HCl environments, has been studied in the oxidation of various compounds by K. Everaert et al [18]. This work is mainly focused on chlorinated VOC but butanol oxidation experiment has also been performed and the activation energy for the butanol is done in comparison with other VOC in the presence of V₂O₅-WO₃/TiO₂ catalyst

73 The present work describes different Zr-Ce-Mn-O catalytic systems synthesized using a sol-
74 gel method. Generally the sol-gel method has been recognized as an interesting way to
75 prepare catalysts with the control of their texture, composition, homogeneity and structural
76 properties [19]. The focus is to optimize the performances of the Zr-Ce-Mn oxides for
77 complete oxidation of n-butanol by examining the effect of Mn amount.

79 Experimental

80 The mixed metal oxides catalysts $Zr_{0.4}Ce_{0.6-x}Mn_xO_2$ ($x = 0; 0.12; 0.24; 0.36; 0.48; 0.60$) were
81 prepared using a sol-gel method. The $ZrO(NO_3)_2 \cdot 5H_2O$, $Ce(NO_3)_3 \cdot 6H_2O$ and
82 $Mn(NO_3)_2 \cdot 5H_2O$ (0.5 mol/L) nitrates were dissolved separately in ethanol and then mixed
83 together in the desired molar ratio of Zr:Ce:Mn. The resulting solution was heated at 80°C
84 and deionized water containing 5 vol. % of ethanol was added to it under constant stirring.
85 The resulting gel was gradually formed after few minutes and the temperature was maintained
86 for 1.5h. The gel was then allowed to mature overnight at room temperature (RT) before
87 being heated at 80°C and 100°C respectively in order to remove ethanol and excess water.
88 After grinding, the resulting powders were calcined by heating from RT to 300°C (2 h) and
89 from 300°C to 500°C (2 h) in flowing air.

90 The powder X-ray diffraction patterns (XRD) of the samples were collected with a D8
91 Advance-BRUKER diffractometer using $Cu K\alpha$ radiation. The diffractograms were recorded
92 with the 2θ range of 10-80° with a step size of 0.02° and a step time of 2 s. The average
93 crystallite size was determined from the Scherrer equation. The lattice parameter was
94 estimated using FullProf software. The nitrogen adsorption and desorption isotherms were
95 measured at -196°C on a Micromeritics ASAP 2010 apparatus. The samples were degassed at
96 160°C for 4h before the measurement. The specific surface area was calculated using the BET
97 model. H_2 -temperature programmed reduction (H_2 -TPR) was investigated (Micromeritics

Autochem II) by heating the samples (50 mg) in H₂ (5 vol.%)/Ar flow (50 mL min⁻¹) at a heating rate of 5°C min⁻¹ from 20 to 900°C.

X-ray photoelectron spectroscopy (XPS) analyses were conducted with Kratos Axis Ultra DLD spectrometer with a monochromatic Al K α (h ν = 1486.6 eV) radiation source operated at 15 kV and 15 mA. The binding energy (BE) was calibrated based on the line position of C 1s (285 eV). CasaXPS processing software was used to estimate the relative abundance of the different species.

The activity of the catalysts (200 mg) was measured in a continuous flow system on a fixed bed reactor at atmospheric pressure and space velocity of 12000 h⁻¹. The flow (100 mL.min⁻¹) of the reactant gases (800 ppm of butanol in air) was adjusted by a Calibrage PUL 010 and DGM 110 apparatus comprising of a saturator and one mass flow controller. The reactor temperature was increased from RT to 400°C (0.5°C min⁻¹). The exit gases were analyzed by a VARIAN 3800 gas chromatograph equipped with a FID for the analysis of the organic reactants and a TCD for the analysis of CO and CO₂.

Results and discussion

XRD patterns of Zr_{0.4}Ce_{0.6-x}Mn_xO₂ samples are displayed in Fig. 1. The pattern of Zr_{0.4}Ce_{0.6}O₂ can be satisfactorily indexed in a fluorite type of structure [20], suggesting the Zr ions incorporation in the cubic lattice to form a homogeneous Zr-Ce-O solid solution. The cubic lattice has been confirmed by Raman spectroscopy. Indeed a strong broad band centered at 480 cm⁻¹ and attributed to the Raman-active F_{2g} mode has been observed for Zr_{0.4}Ce_{0.6}O₂ sample (not shown). Decrease in the lattice parameter *a* from 5.4120 Å for pure CeO₂ [21] to 5.315 (±0.001) Å is observed on the calcined Zr_{0.4}Ce_{0.6}O₂ sample, in accordance with the smaller ionic radius of Zr⁴⁺ ion (0.84Å) compared to that of Ce⁴⁺ (0.97Å). When adding small amounts of manganese, the fluorine-type structure is preserved (Fig. 1). No manganese and

123 zirconium oxide phases are detected on $Zr_{0.4}Ce_{0.48}Mn_{0.12}O_2$ solid. The absence of such phases
124 suggests that Mn and Zr related species may be incorporated into the CeO_2 lattice forming
125 solid solutions [22]. This is also supported by the lower value of the lattice constant a of
126 $Zr_{0.4}Ce_{0.48}Mn_{0.12}O_2$ sample ($5.303 \pm 0.001 \text{ \AA}$) due to the low ionic radius of Mn^{n+} ($Mn^{2+} =$
127 0.83 \AA , $Mn^{3+} = 0.64 \text{ \AA}$, and $Mn^{4+} = 0.53 \text{ \AA}$). Only a broad asymmetric peak in the 2θ range of
128 $25\text{--}35^\circ$ is observed for the $Zr_{0.4}Ce_{0.36}Mn_{0.24}O_2$ sample with a higher Mn content. As the Mn
129 content is further increased, ($Zr_{0.4}Ce_{0.24}Mn_{0.36}O_2$) the same peak is less obvious and appears
130 significantly enlarged. Finally the most enriched Mn sample containing cerium is totally
131 amorphous. Hence with increasing content of manganese in the presence of cerium,
132 amorphous nature of the samples is enhanced. Similar qualitative observations have been
133 reported on Mn-Ce-O composites elsewhere [22,23]. These authors attribute this to the
134 occurrence of more defective fluorite like lattices having a lower degree of crystallinity and a
135 smaller particle size as the sample is enriched with Mn. Compared to Ce-Mn-O systems, the
136 greater degree of amorphous nature in this study could be due to presence of zirconium which
137 retards the crystallization of the samples and/or allows forming some small oxide related
138 crystallites. The XRD pattern of $Zr_{0.4}Mn_{0.6}O_2$ is constituted of peaks attributed to Mn_2O_3
139 phase (JCPDS 41-1442) without any ZrO_2 crystallization.

140
141 The addition of Mn to the Zr-Ce-O system leads to increase in surface area and a
142 corresponding increase and decrease in porous volume and crystallite size respectively as
143 shown in Table 1. The specific surface area doubles on increasing x from 0 to 0.48; the
144 average crystallite size which is 4.5 nm for x= 0 decreases to 1.2 nm for x= 0.36. For x = 0.60,
145 an Mn_2O_3 average crystallite size of 30 nm is measured, the corresponding high specific area
146 can be explained by the formation of amorphous zirconia. Similar systems with nominal
147 composition $Zr_{(0.3)}Ce_{(0.6)}Mn_{(0.1)}O_2$ have been synthesized by a sol-gel method using citric acid

148 as chelating agent [9,24]. Specific surface area of $55 \text{ m}^2 \cdot \text{g}^{-1}$ has been obtained by the authors
149 after a calcination step at 500°C . Then a much higher surface area ($>110 \text{ m}^2 \cdot \text{g}^{-1}$) can be
150 reached using our synthesis procedure. Fig. 2 displays the porous diameter distribution for
151 $\text{Zr}_{(0.4)}\text{Ce}_{(0.6-x)}\text{Mn}_{(x)}\text{O}_2$ samples. A porous diameter distribution centered on 4 nm is found
152 whatever the x value and is stressed for the cerium containing samples. Similar correlation
153 between the BET surface area and average pore radius has been obtained by Fornasiero et al.
154 [20] : for a half specific area ($50 \text{ m}^2 \cdot \text{g}^{-1}$ for $\text{Ce}_{0.6}\text{Zr}_{0.4}\text{O}_2$ mixed oxides prepared by citrate
155 method), a double average pore diameter size (8 nm) has been found.

156
157 Fig. 3 shows the H_2 -TPR profiles of $\text{Zr}_{(0.4)}\text{Ce}_{(0.6-x)}\text{Mn}_{(x)}\text{O}_2$ samples. H_2 -TPR profile of
158 $\text{Zr}_{0.4}\text{Ce}_{0.6}\text{O}_2$ exhibits a main reduction peak centered at 543°C related to the concomitantly
159 reduction of Ce^{4+} ions at the surface and in the bulk of the overall solid solution. The presence
160 in the TPR profile of the shoulder at around 370°C may be related to the presence of some
161 ceria impurity not incorporated in the solid solution [25]. H_2 -TPR curve of $\text{Zr}_{0.4}\text{Mn}_{0.6}\text{O}_2$
162 shows two overlapped strong reduction peaks at 351°C and 454°C . Assuming that +II is the
163 final reduction state of manganese species, the peak at low temperature can be ascribed to the
164 reduction of Mn_2O_3 to Mn_3O_4 . The peak at high temperature corresponds to the reduction of
165 Mn_3O_4 to MnO . Addition of cerium to Zr-Mn solid shifts the reduction temperature of
166 manganese and cerium species to lower temperature. The promotion in the temperature
167 reduction points to the interaction between manganese and cerium species. From $x = 0$ to $x =$
168 0.36 , the reduction onset temperature decreases (Fig. 3), indicating an increase in the oxygen
169 mobility. From $x = 0.36$ to $x = 0.60$, a decrease in oxygen mobility is observed (Table 1 and
170 Fig. 3). Similar results on mesoporous $\text{MnO}_x\text{-CeO}_2$ samples have been observed by Zou et al.
171 [26] and an optimum Mn/Ce ratio of 0.67 has been reported. The total H_2 consumption is
172 listed in Table 1. Assuming that both Mn^{n+} species are reduced completely to Mn^{2+} , Zr^{4+} is

173 not reduced in the temperature range studied, and $\text{Ce}^{3+}/\text{Ce}^{4+}$ bulk molar ratio is unchanged, an
174 average oxidation number (AON) of manganese is obtained for each sample (Table 1). AON
175 value of 3 for $\text{Zr}_{0.4}\text{Mn}_{0.6}\text{O}_2$ matches well with the Mn_2O_3 phase identified by XRD. AON
176 values > 3.2 indicate the presence of Mn^{3+} and Mn^{4+} species mixture in the Zr-Ce-Mn solids.
177
178 The surface XPS values of $\text{Ce}/(\text{Ce}+\text{Mn})$, calculated from the area of the Ce 3d and Mn 2p
179 core levels, are lower than the bulk ratio expected for the $\text{Zr}_{0.4}\text{Ce}_{0.12}\text{Mn}_{0.48}\text{O}_2$ sample (Table
180 2). This can be explained by the formation of manganese-rich oxide phase at the surface. This
181 result has already been observed in Mn-Ce systems [26]. An example of the XPS spectra of
182 Mn 2p, Mn 3s, O 1s and Ce 3d is depicted in Fig. 4. The O 1s core-level spectra have been
183 fitted with two peak contributions, referred to as O_I and O_{II} components (Fig. 4). The major
184 peak O_I with BE of 529.5-529.9 eV is characteristic of lattice oxygen [27,28]. This
185 component O_I is displaced towards higher BE with Mn content increase (Table 2) due to
186 higher BE of lattice oxygen in MnO_x than in CeO_2 [27]. Component O_{II} with BE of 531.2 eV
187 belongs probably to defect oxide, hydroxyl or carbonate groups [28]. The relative abundance
188 of these two kinds of oxygen species is similar for all compositions ($\text{O}_I \sim 63\%$ and $\text{O}_{II} \sim$
189 37%). The Mn 3s peak splitting widths for different Mn oxides are helpful to find out the
190 oxidation state of manganese species [29,30], an Mn 3s splitting width ΔE of 4.8 and 5.4 eV
191 correspond to the presence of Mn^{4+} and Mn^{3+} , respectively. Therefore, Mn^{4+} and Mn^{3+} ions
192 are certainly present together at the surface, since an Mn 3s splitting width ΔE of 5.1-5.2 eV is
193 observed in all the Ce containing samples (Table 2). This is in agreement with an AON > 3.2
194 calculated from the H_2 -TPR data. Mn 3s splitting width ΔE of 5.4 eV is observed in
195 $\text{Zr}_{0.4}\text{Mn}_{0.6}\text{O}_2$, indicating that Mn^{3+} is exclusively formed at the surface when cerium element
196 is absent. This correlates with Mn_2O_3 formation observed in XRD analysis. The BE of Mn
197 2p_{3/2} photopeak is rather broad and the co-existence of Mn^{4+} and Mn^{3+} at the surface can be

198 suggested (Fig. 4). Mn 2p_{3/2} peak can be split in two components which give reasonable
199 fitting with BE of 643.4 eV and 641.8 eV for Mn⁴⁺ and Mn³⁺, respectively. These values are
200 found to be higher than those recorded from pure MnO₂ and Mn₂O₃, probably due the strong
201 interaction between manganese, cerium and zirconium oxides. Clearly with increasing Mn,
202 the relative concentration of Mn⁴⁺ increases from 34% to 40% (Table 2). The same
203 observation has been reported on MnO_x-CeO₂ mixed oxides [8]. The Ce 3d spectra of Ce⁴⁺
204 and Ce³⁺ can be resolved into six and four components, respectively [31]. The Ce 3d_{5/2} BE in
205 ceria is found close to 882.0 eV. Addition of zirconium and manganese to ceria causes an
206 upper shift of 0.3 – 0.4 eV which can be considered as a direct evidence for solid solution
207 formation. The relative abundance of Ce⁴⁺ present in the solid is assessed through the
208 calculation of the percentage of the area under the Ce⁴⁺ u''' (916.7 eV) relative to the total
209 area under the Ce 3d spectral envelop using the method proposed by Shyu et al. [32].
210 Addition of a small amount of Mn causes an increase in the surface Ce⁴⁺ concentration since
211 u''' intensity goes from 14% to 16%. But with further Mn content increase, the concentration
212 of Ce⁴⁺ decreases (Table 2). This result can be explained by an electrons transfer from Mn to
213 Ce, since in parallel, Mn⁴⁺ concentration increases. In Mn-Ce-O composites, Chen et al. [23]
214 suggested an electron transfer but from Ce to Mn since addition of manganese to cerium
215 increased the abundance of surface Ce⁴⁺ species.

216
217 The single carbon-containing product of butanol oxidation is CO₂ at high conversion levels.
218 Butanal is the major intermediate product in the course of butanol oxidation towards CO₂,
219 other aldehydes such as propanal and ethanal are detected but in negligible concentrations.
220 Fig. 5A presents the conversion of butanol to butanal over Zr_(0.4)Ce_(0.6-x)Mn_(x)O₂ catalysts. Mn
221 addition to Zr-Ce system causes the formation of butanal at lower temperatures. Without
222 cerium, the maximum of butanal yield is shifted to higher temperatures. These results are in

223 line with the redox properties changes. It is well known that alcohol catalytic oxidation
224 provides reaction intermediates such as aldehydes, ketons and acetic acids [11]. The major
225 path appears to be the direct oxidation of butanal to CO₂; its oxidation via the acid is expected
226 to be a minor path, because (1) no butanoic acid is detected and (2) CO₂ starts to be produced
227 when the butanal concentration decreases. The same reaction scheme “butanol → butanal →
228 CO₂” has already been observed during the homogeneous oxidation of 150 ppm of butanol in
229 air [16]. The homogeneous conversion of butanol to butanal is maximized at around 260°C
230 whereas the maximum is lowered to 125°C in the presence of Zr_{0.4}Ce_{0.6-x}Mn_xO₂ solid
231 solutions.

232 Fig. 5B shows the butanol conversion over Zr_(0.4)Ce_(0.6-x)Mn_(x)O₂ catalysts as a function of
233 reaction temperature. From x = 0 to x = 0.24, the catalytic activity increases with Mn addition.
234 For x ≥ 0.36, the catalytic activity is similar, indicating that the optimal composition is
235 obtained for Zr_{0.4}Ce_{0.24}Mn_{0.36}O₂. For these compositions, 90% of butanol is transformed at
236 about 175°C (Fig. 5B). Despite the high quantity of manganese, the activity of Zr_{0.4}Mn_{0.60}O₂
237 is not the highest. This result can be correlated to the absence of Ce⁴⁺/Ce³⁺ and Mn⁴⁺/Mn³⁺
238 redox couples. Indeed the redox properties of catalysts are known to govern the catalytic
239 activity in the total VOC oxidation [5,33]. These results can be connected with (i) the oxygen
240 mobility and (ii) the surface Mn⁴⁺ concentration, both maximum for x = 0.36 value (Table 2).

241 With similar space velocity (15000 h⁻¹) and over a monolith Pt/Al₂O₃ catalyst, conversion of
242 butanol higher than 90% was obtained in the 180-200°C temperature range by Hermia and
243 Vigneron [34]. With a double space velocity and over Co, Pd, Pt supported on γ alumina (the
244 majority of commercial catalysts consists of Pt or Pd supported on alumina supports), 90% of
245 butanol is transformed at 220°C, 220°C and 180°C, respectively [16]. This comparison with
246 commercial catalysts illustrates the excellent behaviour of the Zr_{0.4}Ce_{0.6-x}Mn_xO₂ catalytic

247 system for oxygenated VOC removal since n-butanol conversion of 90% is obtained at 175°C
1
2 248 for $x = 0.36$ value.

3
4
5 249

6 7 250 **Conclusion**

8
9 251 $Zr_{0.4}Ce_{0.6-x}Mn_xO_2$ solid solutions were successfully synthesized by a sol-gel method,
10
11 252 characterized and tested for the total oxidation of butanol. The catalytic results were mainly
12
13 253 explained by the textural (SSA and crystallite size), and bulk/surface properties (oxygen
14
15 254 mobility and Mn^{4+} concentration). The presence of both Ce^{4+}/Ce^{3+} and Mn^{4+}/Mn^{3+} redox
16
17 255 couples led to excellent catalytic activity for butanol complete oxidation with an activity
18
19 256 maximum for $x = 0.36$.

20 21 22 257 **Acknowledgements**

23
24
25 258 The authors thank the European Community and the Region “Nord Pas de Calais” for
26
27 259 financial supports through Interreg IV “Redugaz” and IRENI projects.

28 29 30 260 31 32 261 **References**

- 33
34
35 262 [1] J. Carpentier, J.-F. Lamonier, S. Siffert, E. A. Zhilinskaya and A. Aboukaïs,
36
37 263 Characterisation of Mg/Al hydrotalcite with interlayer palladium complex for catalytic
38
39 264 oxidation of toluene, *Appl. Catal. A Gen.* **234** (2002), pp. 91-101.
40
41 265 [2] P. Papaefthimiou, T. Ioannides and X. E. Verykios, VOC removal: investigation of
42
43 266 ethylacetate oxidation over supported Pt catalysts, *Catal. Today* **54** (1999), pp. 81–92.
44
45 267 [3] F. Wyrwalski, J.-F. Lamonier, S. Siffert and A. Aboukaïs, Additional effects of cobalt
46
47 268 precursor and zirconia support modifications for the design of efficient VOC oxidation
48
49 269 catalysts, *Appl. Catal. B: Environ.* **70** (2007), pp. 393-399.
50
51 270 [4] A. Gervasini, G. C. Vezzoli and V. Ragaini, VOC removal by synergic effect of
52
53 271 combustion catalyst and ozone, *Catal. Today* **29** (1996), pp. 449-455.
54
55 272 [5] B. Aellach, A. Ezzamarty, J. Leglise, C. Lamonier and J.-F. Lamonier, Calcium-Deficient
56
57 273 and Stoichiometric Hydroxyapatites Promoted by Cobalt for the Catalytic Removal of
58
59 274 Oxygenated Volatile Organic Compounds, *Catal. Lett.* **135** (2010), pp. 197-206.

- 275 [6] L. Lamaita, M. A. Peluso, J. E. Sambeth, H. J. Thomas, Synthesis and characterization of
1 276 manganese oxides employed in VOCs abatement, *Appl. Catal. B: Environ.* **61** (2005), pp.
3 277 114-119.
- 5 278 [7] J. Luo, Q. Zhang, A. Huang, S. L. Suib, Total oxidation of volatile organic compounds
6 279 with hydrophobic cryptomelane-type octahedral molecular sieves, *Microporous Mesoporous*
8 280 *Mater.* **35-36** (2000), pp 209-217.
- 10 281 [8] W. Xingyi, K. Qian and L. Dao, Catalytic combustion of chlorobenzene over MnO_x-CeO₂
12 282 mixed oxide catalysts, *Appl. Catal. B: Environ.* **86** (2009), pp. 166-175.
- 14 283 [9] T. Rao, M. Shen, L. Jia, J. Hao and J. Wang, Oxidation of ethanol over Mn-Ce-O and
15 284 Mn-Ce-Zr-O complex compounds synthesized by sol-gel method, *Catal. Comm.* **8** (2007),
17 285 pp. 1743-1747.
- 19 286 [10] S. Hamoudi, F. Larachi, A. Adnot and A. Sayari, Characterization of Spent MnO₂/CeO₂
21 287 Wet Oxidation Catalyst by TPO-MS, XPS, and S-SIMS, *J. Catal.* **185** (1999), pp. 333-344.
- 23 288 [11] D. Delimaris and T. Ionnides, VOC oxidation over MnO_x-CeO₂ catalysts prepared by a
24 289 combustion method, *Appl. Catal. B.* **84** (2008), pp. 303-312.
- 26 290 [12] A.M.T. Silva, R.R.N Marques and R.M. Quinta-Ferreira, Catalysts based in cerium oxide
28 291 for wet oxidation of acrylic acid in the prevention of environmental risks, *Appl. Catal. B.* **47**
30 292 (2004), pp. 269-279.
- 32 293 [13] C.E. Hori, H. Permana, K. Y. S. Ng, A. Brenner, K. More, K. M. Rahmoeller and D.
34 294 Belton, Thermal stability of oxygen storage properties in a mixed CeO₂-ZrO₂ system, *Appl.*
35 295 *Catal. B: Environ.* **16** (1998), pp. 105-117.
- 37 296 [14] U.S. Environmental Protection Agency's Integrated Risk Information System (IRIS).
38 297 Summary on n-Butanol (71-36-3), <http://www.epa.gov/iris/>
- 40 298 [15] G. D. Clayton, F.E. Clayton (eds.), Patty's Industrial Hygiene and Toxicology, **2A, 2B,**
41 299 **2C, 2D, 2E, 2F: Toxicology. 4th ed. New York, NY : John Wiley & Sons Inc.** (1993-1994), pp.
42 300 2639-2640 .
- 44 301 [16] P. Papaefthimiou, T. Ioannides, X. E. Verykios, Combustion of non-halogenated volatile
45 302 organic compounds over group VIII metal catalysts, *Appl. Catal. B: Environ.* **13** (1997), pp.
46 303 175-184.
- 48 304 [17] P. Papaefthimiou, T. Ioannides, X. E. Verykios, Catalytic incineration of volatile organic
49 305 compounds present in industrial waste streams, *Appl. Therm. Eng.* **18** (1998), pp. 1005-1012.
- 51 306 [18] K. Everaert, J. Baeyens, Catalytic combustion of volatile organic compounds, *J. Hazard.*
52 307 *Mater.* **B109** (2004), pp. 113-139.

- 308 [19] M. A. Cauqui, J. M. Rodriguez-Izquierdo, Application of the sol-gel methods to catalyst
1 309 preparation, *J. Non-Cryst. Solids* **147/148** (1992), pp. 724-738.
- 3 310 [20] P. Fornasiero, E. Fonda, R. Di Monte, G. Vlaic, J. Kaspar and M. Graziani, Relationships
4 311 between structural/textural properties and redox behavior in $\text{Ce}_{0.6}\text{Zr}_{0.4}\text{O}_2$ mixed oxides, *J.*
5 312 *Catal.* **187** (1999), pp. 177-185.
- 7 313 [21] M. Wolcyrz and L. Kepinski, Rietveld refinement of the structure of CeOCl formed in
8 314 Pd/CeO₂ catalyst: Notes on the existence of a stabilized tetragonal phase of La₂O₃ in La-Pd-O
9 315 system, *J. Solid State Chem.* **99** (1992), pp. 409-413.
- 11 316 [22] G. Picasso, M. Gutiérrez, M. P. Pina and J. Herguido, Preparation and characterization of
12 317 Ce-Zr and Ce-Mn based oxides for *n*-hexane combustion: Application to catalytic membrane
13 318 reactors, *Chem. Eng. J.* **126** (2007), pp. 119-130.
- 14 319 [23] H. Chen, A. Sayari, A. Adnot and F. Larachi, Composition–activity effects of Mn–Ce–O
15 320 composites on phenol catalytic wet oxidation, *Appl. Catal. B: Env.* **32** (2001), pp. 195-204.
- 16 321 [24] L. Jia, M. Shen, J. Wang, X. Chu, J. Wang and Z. Hu, Redox behaviors and structural
17 322 characteristics of $\text{Mn}_{0.1}\text{Ce}_{0.9}\text{O}_x$ and $\text{Mn}_{0.1}\text{Ce}_{0.6}\text{Zr}_{0.3}\text{O}_x$, *J. Rare Earth.* **26** (2008), pp. 523-527.
- 18 323 [25] L. F. Liotta, A. Longo, G. Pantaleo, G. Di Carlo, A. Martorana, S. Cimino, G. Russo and
19 324 G. Deganello, Alumina supported Pt(1%)/ $\text{Ce}_{0.6}\text{Zr}_{0.4}\text{O}_2$ monolith : remarkable stabilization of
20 325 ceria-zirconia solution towards CeAlO₃ formation operated by Pt under redox conditions,
21 326 *Appl. Catal. B: Env.* **90** (2009), pp. 470-477.
- 22 327 [26] Z.-Q. Zou, M. Meng and Y.-Q. Zha, Surfactant-Assisted Synthesis, Characterizations,
23 328 and Catalytic Oxidation Mechanisms of the Mesoporous MnOx–CeO₂ and Pd/MnOx–CeO₂
24 329 Catalysts Used for CO and C₃H₈ Oxidation, *J. Phys. Chem.* **114** (2010), pp. 468-477.
- 25 330 [27] M. Machida, M. Uto, D. Kurogi and T. Kijima, MnOx–CeO₂ Binary Oxides for Catalytic
26 331 NO_x Sorption at Low Temperatures. Sorptive Removal of NO_x, *Chem. Mater.* **12** (2000), pp.
27 332 3158-3164.
- 28 333 [28] F. Larachi, J. Pierre, A. Adnot and A. Bernis, Ce 3d XPS study of composite
29 334 $\text{Ce}_x\text{Mn}_{1-x}\text{O}_{2-y}$ wet oxidation catalysts, *Appl. Surf. Sci.* **195** (2002), pp. 236-250.
- 30 335 [29] B. Djurfors, J. N. Broughton, M. J. Brett and D. G. Ivey, Electrochemical oxidation of
31 336 Mn/MnO films: formation of an electrochemical capacitor, *Acta Mater.* **53** (2005), pp. 957-
32 337 965.
- 33 338 [30] M. Toupin, T. Brousse and D. Bélanger, Influence of Microstructure on the Charge
34 339 Storage Properties of Chemically Synthesized Manganese Dioxide, *Chem. Mater.* **14** (2002),
35 340 pp. 3946-3952.

341 [31] A. Laachir, V. Perrichon, A. Badri, J. Lamotte, E. Catherine, J. C. Lavalley, J. El Fallah,
1 342 L. Hilaire, F. Le Normand, E. Quéméré, G. N. Sauvion and O. Touret, Reduction of CeO₂ by
2 343 hydrogen. Magnetic susceptibility and Fourier-transform infrared, ultraviolet and X-ray
3 344 photoelectron spectroscopy measurements, *J. Chem. Soc., Faraday Trans.* **87** (1991), pp.
4 345 1601-1609.

5 346 [32] J. Z. Shyu, W. H. Weber and H. S. Gandhi, Surface characterization of alumina-
6 347 supported ceria, *J. Phys. Chem.* **92** (1988), pp. 4964-4970.

7 348 [33] F. Wyrwalski, J.-M. Giraudon and J.-F. Lamonier, Synergistic Coupling of the Redox
8 349 Properties of Supports and Cobalt Oxide Co₃O₄ for the Complete Oxidation of Volatile
9 350 Organic Compounds, *Catal. Lett.* **137** (2010), pp. 141-149.

10 351 [34] J. Hermia and S. Vigneron, Catalytic incineration for odour abatement and VOC
11 352 destruction, *Catal. Today* **17** (1993), pp. 349-358.

12 353

13 354 **Figure captions**

14 355 Fig. 1 : XRD patterns of Zr_(0.4)Ce_(0.6-x)Mn_(x)O₂ solids

15 356 Fig. 2 : Pore size distribution of Zr_(0.4)Ce_(0.6-x)Mn_(x)O₂ solids

16 357 Fig. 3 : H₂-TPR of of Zr_(0.4)Ce_(0.6-x)Mn_(x)O₂ solids

17 358 Fig. 4 : XPS spectra of Ce 3d, O 1s, Mn 2p and Mn 3s core levels in Zr_{0.40}Ce_{0.12}Mn_{0.48}O₂.

18 359 Fig. 5 : Catalytic results in butanol oxidation A) yield of butanal (%) and B) butanol
19 360 conversion (%) as a function of reaction temperature

Table 1 : textural and redox properties of $Zr_{0.4}Ce_{0.6-x}Mn_xO_2$ samples

Samples	Average crystallite size /nm	Specific surface area / $m^2 g^{-1}$	V_p / $cm^3 g^{-1}$	H_2 consumption / $\mu mol.g^{-1}$	Onset temperature / $^{\circ}C$	Average oxidation number of Mn
$Zr_{0.4}Ce_{0.6}O_2$	4.5	98	0.087	957	280	-
$Zr_{0.4}Ce_{0.48}Mn_{0.12}O_2$	2.8	110	0.084	1700	93	3.8
$Zr_{0.4}Ce_{0.36}Mn_{0.24}O_2$	1.2	157	0.124	2423	82	3.7
$Zr_{0.4}Ce_{0.24}Mn_{0.36}O_2$	1.2	163	0.130	2880	80	3.4
$Zr_{0.4}Ce_{0.12}Mn_{0.48}O_2$	-	199	0.146	3467	90	3.2
$Zr_{0.4}Mn_{0.60}O_2$	30.6	167	0.093	3579	86	3.0

Table 2: data obtained from XPS analyses of $Zr_{0.4}Ce_{0.6-x}Mn_xO_2$ samples

Samples	$\left(\frac{Ce}{Ce + Mn}\right)_{Bulk}$	$\left(\frac{Ce}{Ce + Mn}\right)_{XPS}$	O 1s BE /eV		$\Delta E_{Mn\ 3s}$ /eV	% u''''	Mn 2p	
			O _I	O _{II}			% Mn ³⁺	% Mn ⁴⁺
$Zr_{0.4}Ce_{0.6}O_2$	1.00	1.00	529.5	531.2	-	14	-	-
$Zr_{0.4}Ce_{0.48}Mn_{0.12}O_2$	0.79	0.60	529.6	531.2	5.2	16	66	34
$Zr_{0.4}Ce_{0.36}Mn_{0.24}O_2$	0.58	0.42	529.7	531.2	5.1	15	64	36
$Zr_{0.4}Ce_{0.24}Mn_{0.36}O_2$	0.45	0.28	529.8	531.2	5.1	13	60	40
$Zr_{0.4}Ce_{0.12}Mn_{0.48}O_2$	0.19	0.19	529.8	531.4	5.1	11	60	40
$Zr_{0.4}Mn_{0.60}O_2$	-	-	529.9	531.5	5.4	-	100	-

Fig. 1

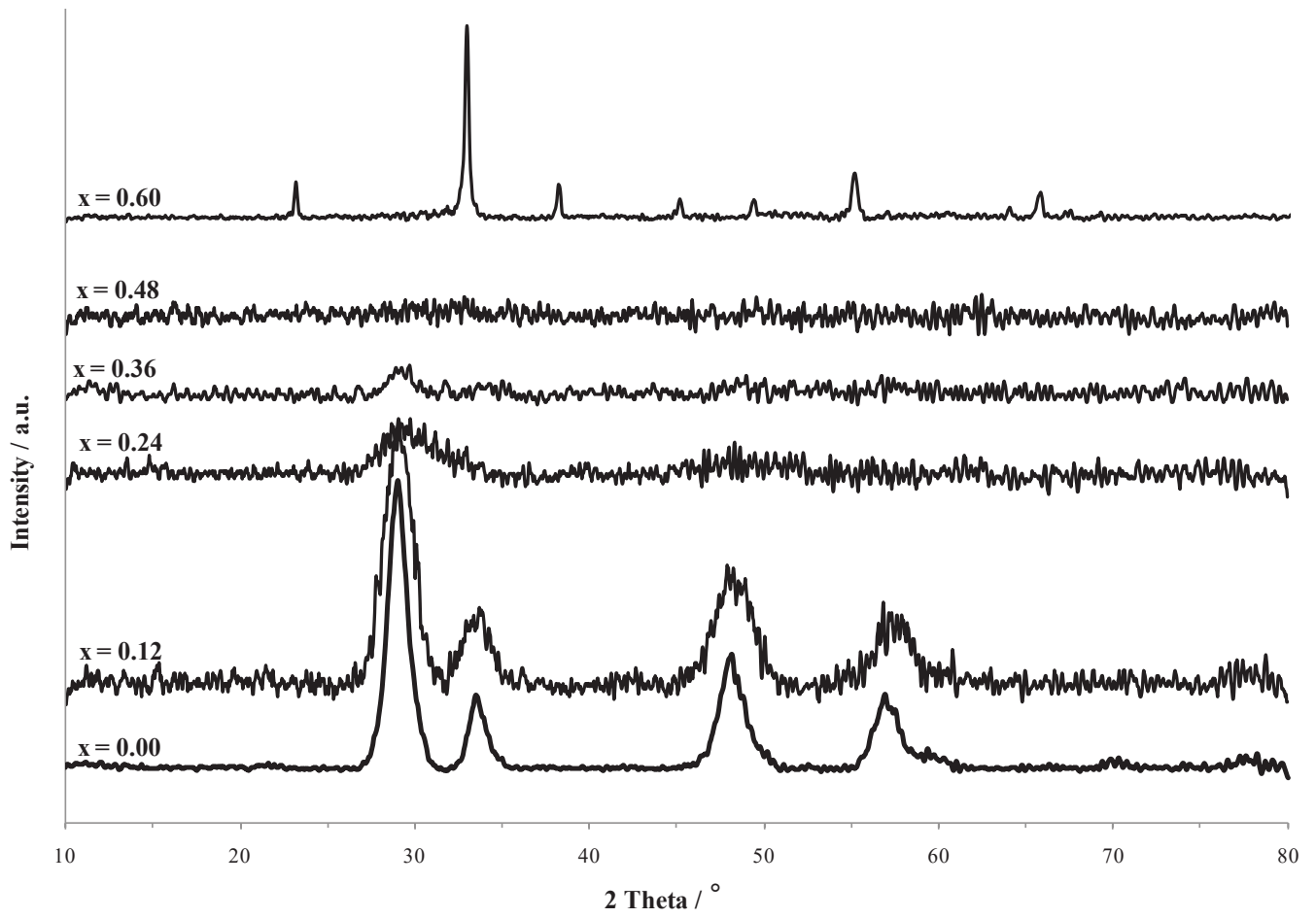


Fig. 2

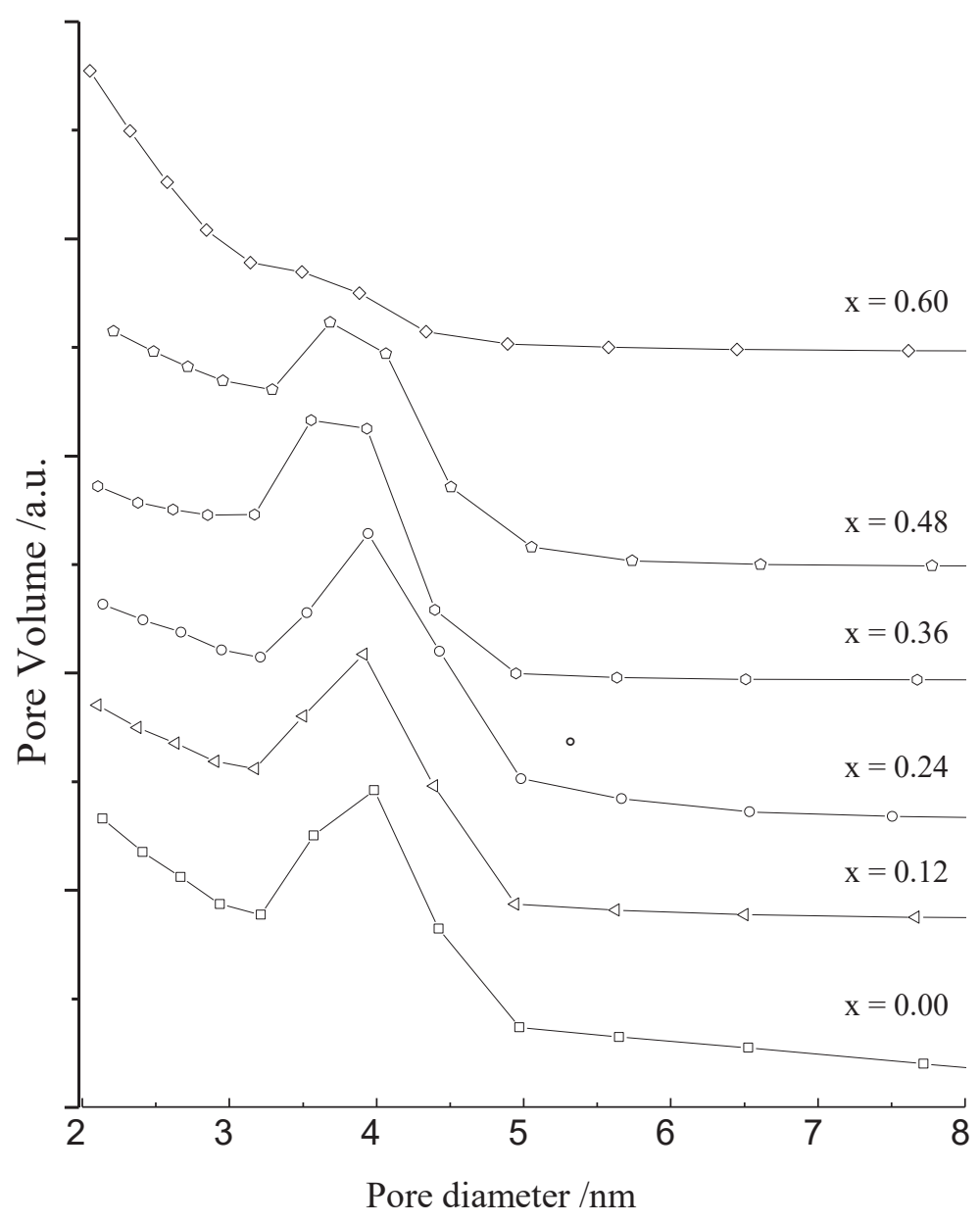
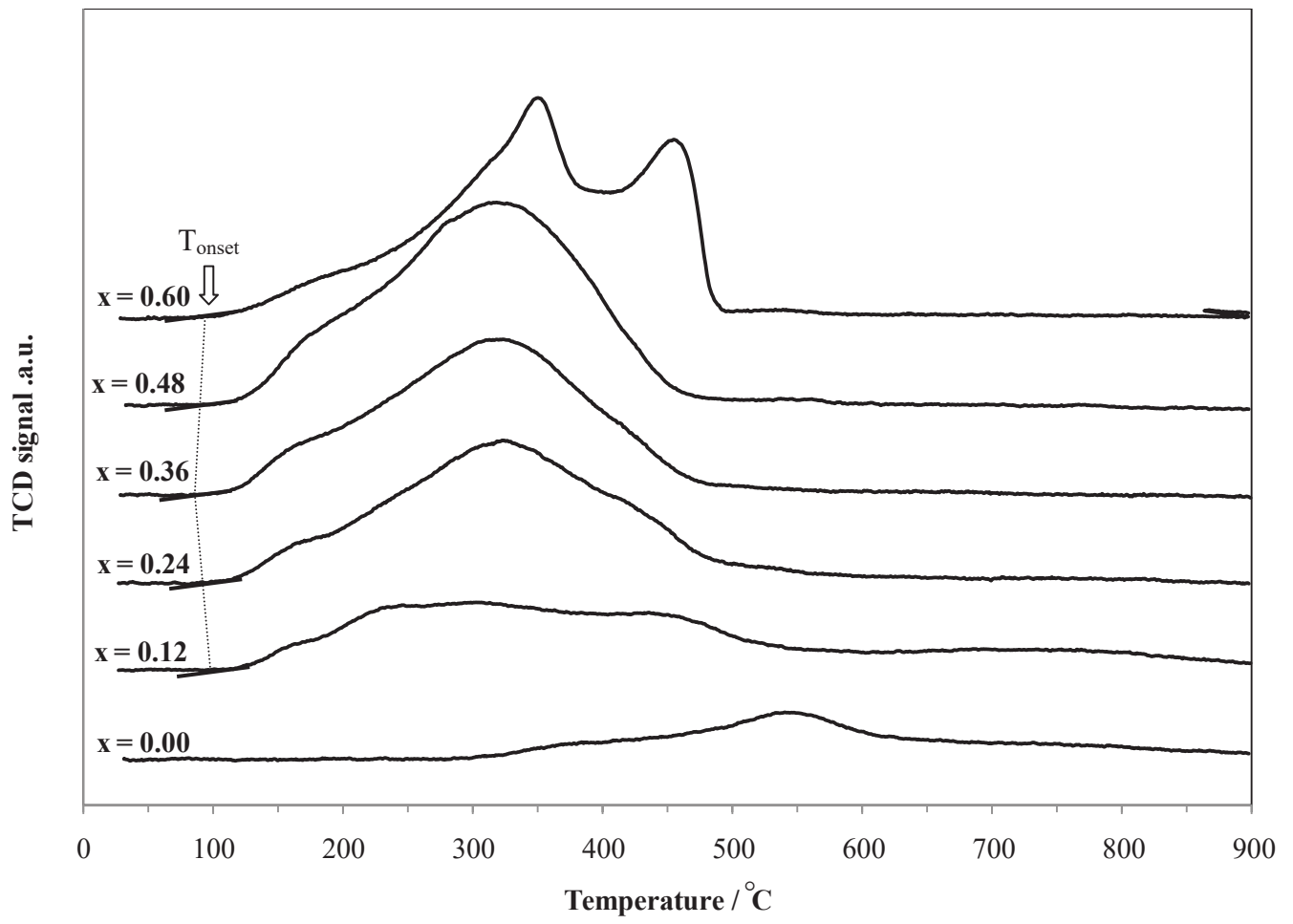


Fig. 3



Figure(s)

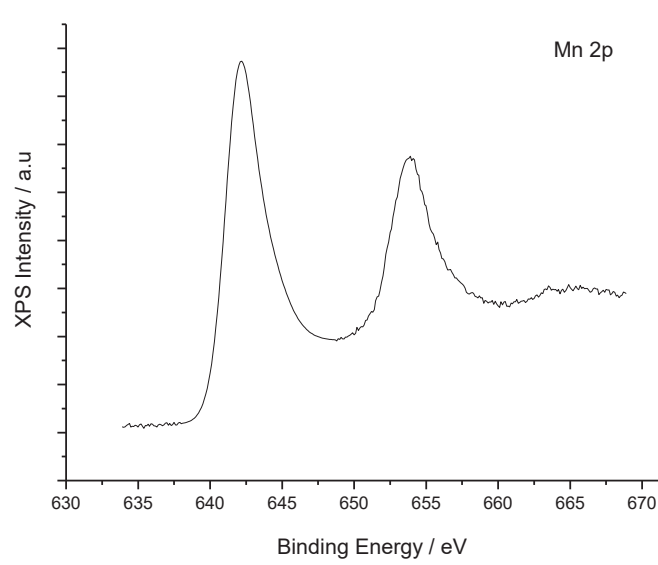
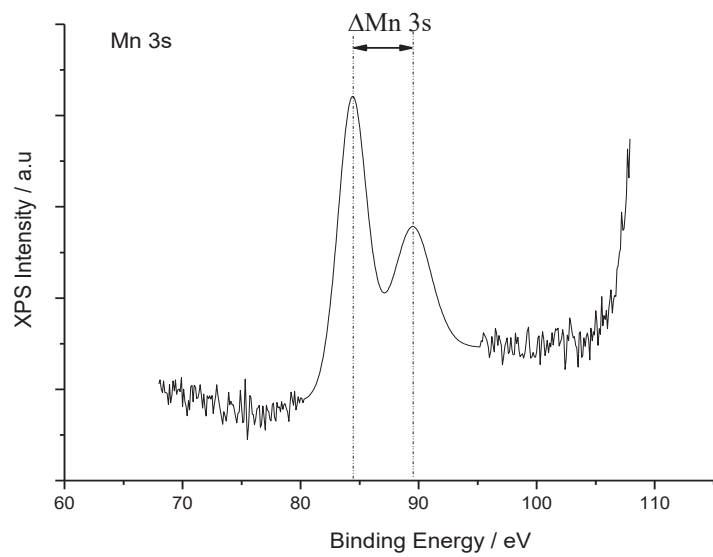
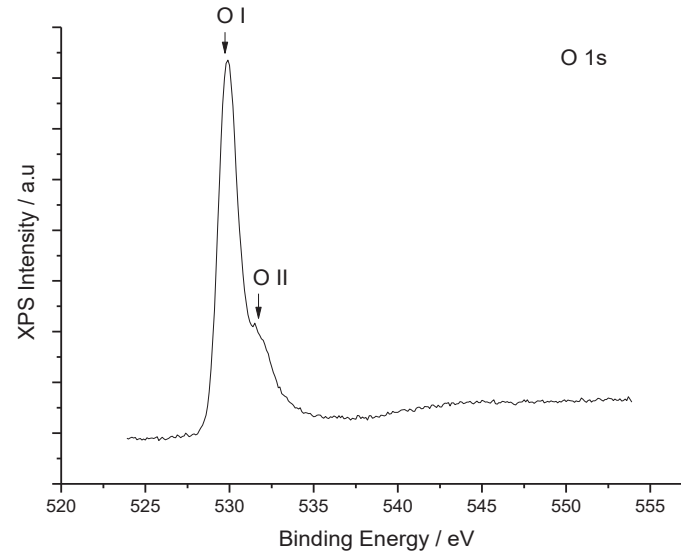
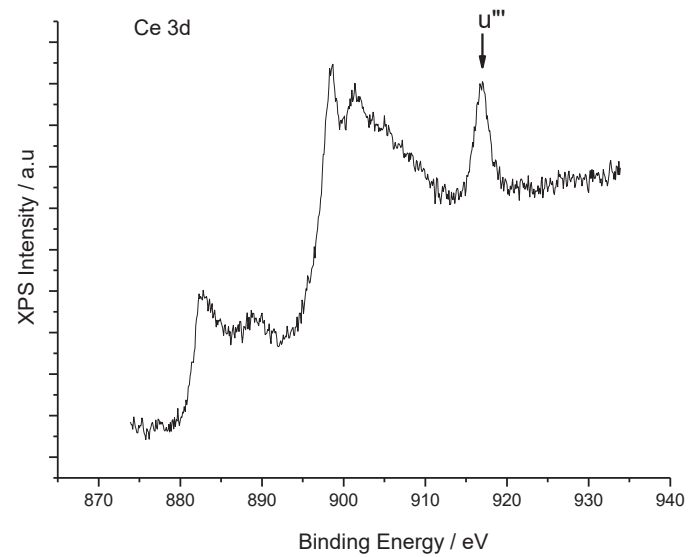
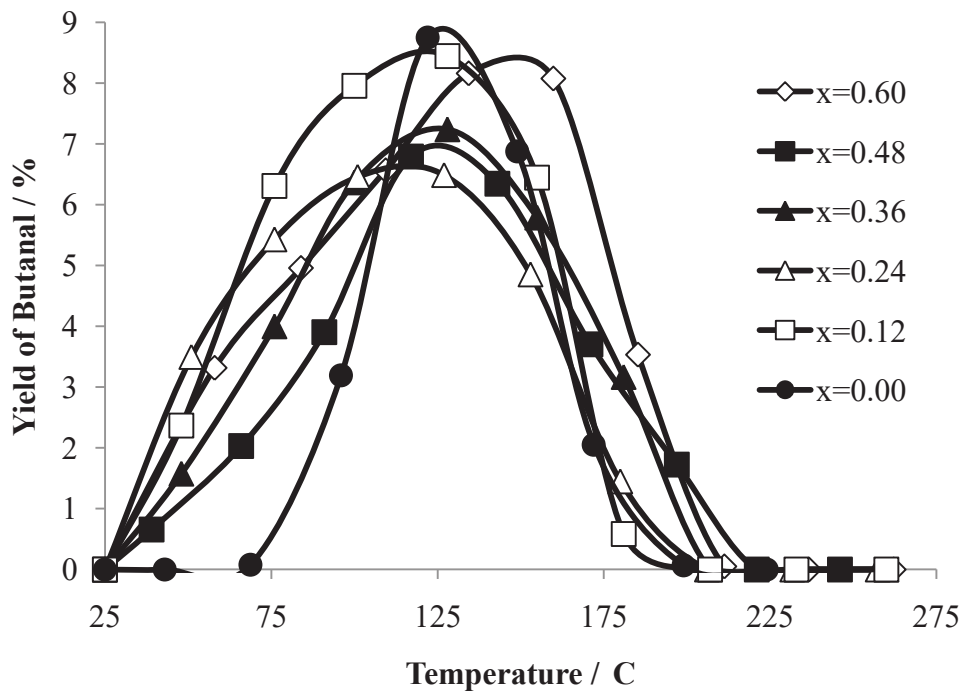


Fig. 4.

Fig. 5

A



B

